

# Origami-Inspired Design of a Hydraulic Tele-Micromanipulation System

Sehyuk Yim, Shuhei Miyashita, Daniela Rus, and Sangbae Kim

## Abstract

*Origami-engineering is an emerging design and manufacturing technology for creating three-dimensional robotic systems using two-dimensional designs. We present a new micromanipulation system featuring origami-inspired minimal design and hydraulic teleoperation. Operators move wearable user-interface-devices on their fingers to control a multi degree-of-freedom micromanipulator where a simple hydraulic system using syringes of different diameters allows motion reduction and force transmission between the master (finger exoskeletons) and the slave (manipulator). The paper presents design considerations and features for creating the origami-based hydraulic tele-micromanipulation system using inexpensive paper cardboards and disposable syringes. Finally, a range of different high level micromanipulation abilities such as trajectory following, pick-and-place, micro-separation, and 3D micro-assembly are demonstrated. Highlighting rapid design and fabrication of a low-cost precision micromanipulation system, this paper proposes new applications of origami-inspired robots to wearable robots and micro robotic manipulation.*

## 1. Introduction

Traditional robots are complex electro-mechanical systems consisting of sensors, actuators, and mechanical structures, controlled by a programmable computer. Thus, developing functional robotic systems is very expensive from time and cost perspectives. The printable programmable robot paradigm is an emerging technology for creating three-dimensional robotic systems using two-dimensional features (Mehta et al., 2014; Onal et al., 2011). This technical approach allows rapid design and fabrication of mass-producible and customizable miniature robotic systems. As a result, different origami-based robotic systems such as autonomous hexapod robots (Soltero et al., 2013), inchworm robots (Felton et al., 2013), thermally-actuated programmable matter (Hawkes et al., 2010), a miniature quad-rotor (Mehta et al., 2013), and thermally activated, configurable electric devices are proposed (An et al., 2014; Felton et al., 2014; Miyashita et al., 2014; Tolley et al., 2014).

Previously, we introduced a paper-made tele-micromanipulation system and its preliminary results, highlighting new applications of origami-inspired robots to wearable devices and micro robotic manipulation (Yim and Kim et al., 2015). Micromanipulation is the key technology for applications in micro-manufacturing (Bhattacharyya et al., 2001; Shimada et al., 2000), micro-assembly (Popa et al., 2004; Thompson et al., 2001), clinical micro-surgery (Yasargil et al., 2006; Boecks et al., 1976), cell manipulation (Gauthier et al., 2006; Tabares et al., 2010), and biomedical engineering research (Causa et al., 2007; Inoue et al., 2005). However, the working ranges and resolution of commercial micromanipulators are set for several target applications such as transgenics (Kawase et al., 2001; Caron et al., 2000), neuroscience (Rebec et al., 1993; Tan et al., 1993), and in-vitro fertilization (Steirteghem et al., 1994). Also, those systems consist of very expensive electric motors or piezoelectric

actuators, gears, precision linear stages, and user-interface-devices. In this paper, we present an advanced origami-inspired hydraulic tele-micromanipulation system with detailed analysis and quantified experimental results. The proposed micromanipulation system is easy-to-design in a computer-aided-design program, easy-to-make by using a laser cutting machine, cost-effective because it is made of low-cost paper cardboards and disposable syringes, and its working range and resolution are customizable by changing the motion reduction ratio of the hydraulic system.

This paper contributes the following four aspects:

- This is the first origami-based tele-micromanipulation system where both the wearable user-interface-devices and the slave manipulator are manufactured by printing and folding.
- This paper presents key origami elements for the precise linear motion of the slave micromanipulator. These elements are also useful in designing other origami-based devices requiring precise motion.
- The minimal ergonomic designs of finger exoskeleton interfaces are expandable to other wearable devices or human-machine interface devices.
- We developed a crease pattern design method for integrating multiple single-sided foldable structures into one pattern. As a result, each origami-based device consisting of complex three-dimensional mechanisms is manufactured from one single paper cardboard where flexure hinges and rigid frames are easily implemented using the thick material.

The paper is organized as follows. Section 2 describes the overall manipulation system. Section 3 and 4 introduce the design features, considerations and manufacturing methods of the finger exoskeletons and the micromanipulator, respectively. Section 5 evaluates the motion precision of the manipulation system quantitatively, and demonstrates different manipulation abilities. In Section 6, the contribution and limitations of the current system are discussed.

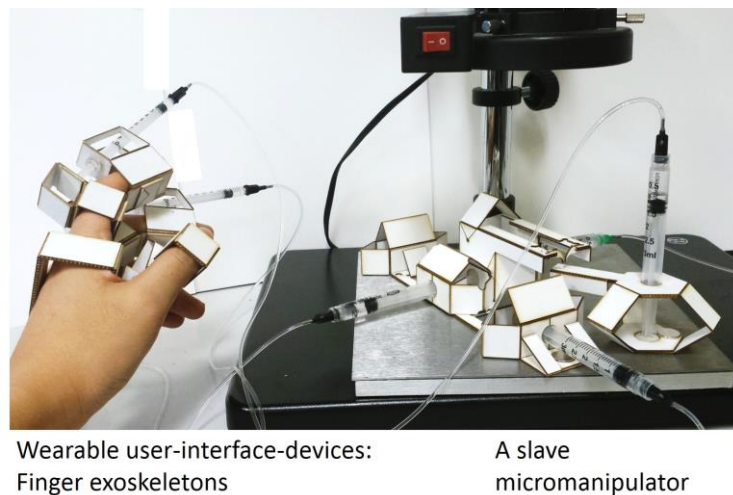


**Fig. 1.** A photograph of the origami-inspired hydraulic tele-micromanipulation system consisting of the paper-made finger exoskeletons (left) and micromanipulator (right). Operators move wearable user-interface-devices on their fingers to control the micromanipulator. The hydraulic system using syringes of different diameters allows motion reduction and force transmission between the master (finger exoskeletons) and the slave (manipulator).

## 2. System Overview

The developed micromanipulation system consists of hydraulically connected two mechanical systems. One is the finger exoskeletons that users control like user-interface-devices (master), and the other is the micromanipulator acting as a slave. Figure 2 shows a schematic diagram of the system. The motion of the finger exoskeleton synchronized with each finger is reduced in the manipulator domain via the hydraulic motion reduction system using two syringes of different diameters where the motion reduction ratio is determined by the cross-sectional area ratio of the syringes. Four finger exoskeletons are required to produce the manipulator's  $x$ -,  $y$ -,  $z$ - motions and the grippers' motion. As a result, operators can pick and place micro objects in a three-dimensional space with the wearable user-interface-devices on their fingers, monitoring the positions of the micro objects and the motion of the manipulator tip in displayed video images. Table 1 shows the specifications of the micromanipulator and finger exoskeletons.

**Table 1.** Specifications of the manipulator and interface devices.

<i>Micromanipulator</i>	
degree-of-freedom	4 ( $x, y, z$ , and $g$ -motions)
workspace ( $x \times y \times z$ )	$< 7 \times 7 \times 10 \text{ mm}^3$
main materials	paper cardboard (thickness: 1.2 mm, <i>Blick</i> , US)
height ( $z$ -axis)	70 mm
length ( $x$ -axis)	250 mm
width ( $y$ -axis)	60 mm
weight	50.7g
embedded syringe	$3 \text{ cm}^3$
<i>Finger exoskeletons</i>	
rotational angle range (thumb)	$30^\circ - 85^\circ$
maximum motion distance (index and middle)	$< 20 \text{ mm}$
main materials	paper cardboard
weight	18g
Embedded syringe	$1 \text{ cm}^3$

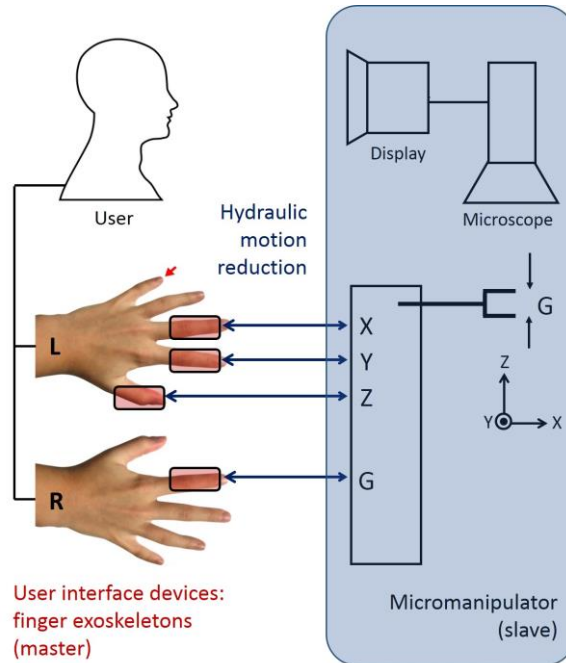


**Fig. 2.** A schematic diagram of the developed hydraulic tele-micromanipulation system. The middle, index and thumb fingers of the left hand (section 3) move the manipulator tip in the  $x$ -,  $y$ -, and  $z$ -directions using linear motion stages (section 4.1), respectively, and the index finger of the right hand controls grippers (section 4.2). The motions of the finger exoskeletons are reduced in the micromanipulator domain by the hydraulic motion reduction system (section 4.3). The microscope above the manipulator and a monitor provide the display for visual feedback to the human operator.

### 3. Wearable user-interface-devices: paper-made finger exoskeletons

#### 3.1. Motion Mapping Strategy

Human fingers are excellent biomechanical systems for interfacing with machines because their dense and sensitive muscular system allows for precise and dexterous control of their motions. The user-interface-devices of the micromanipulation system are wearable on thumb, index, and middle fingers (Fig. 3). The bending angles ( $\alpha$ ,  $\beta$ , and  $\gamma$ ) of the three finger modules correspond to the 3D position ( $x$ ,  $y$ , and  $z$ ) of the manipulator tip. This motion mapping strategy presents that the 3-D motion of the manipulator is decomposed into three 1D motions, which are independently controlled by multiple user-interface-devices.

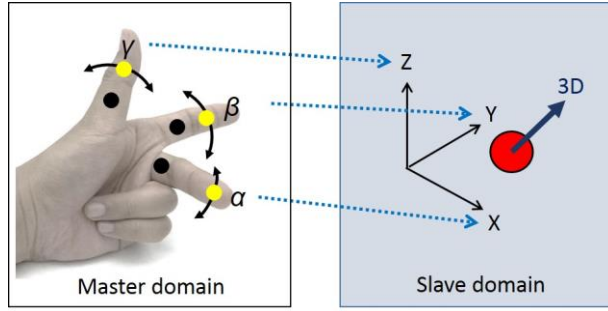


**Fig. 3.** Motion mapping between the finger exoskeletons in the master domain and the micromanipulator tip in the slave domain. The 3D motion of the manipulator tip is controlled by the three fingers' bending motions. The black dots and the yellow dots mean the reference points and the moving points, respectively. The blue dotted arrows indicate the corresponding pairs.

### 3.2. Index and Middle Finger Exoskeletons

Each finger exoskeleton device has one degree-of-freedom motion to implement the motion mapping strategy in Fig. 3. We designed the finger exoskeletons considering the ergonomics of fingers. Figure 4(a)-(b) shows the design and motion of the index (and/or middle) finger exoskeleton. One rigid rectangular parallelepiped holds the proximal phalanx, which becomes the reference. If the finger is bent by contracting the flexor muscle, the distal phalanx (or the middle one) slightly slides in the second rectangular parallelepiped in its length direction, pressing the bottom surface in the normal direction. The expanding syringe draws water from the other syringe in the manipulator (Section 4.3 details this hydraulic mechanism). If the finger is relaxed by contracting the extensor muscle, the produced torque compresses the syringe piston and pushes water to the manipulator syringe where the two phalanx holders are connected by the point of lever. Figure 5 shows the free-body-diagram of the exoskeleton to obtain analytical equations about the motion and force relation. The linear displacement of the syringe piston is expressed as

$$d_m = 2r \sin\left(\frac{\theta_m}{2}\right) \quad (1)$$

where  $\theta_m$  is the angle between two phalanx holders,  $r$  is the height of the finger holder, and  $d_m$  is the distance between two surfaces  $P_1$  and  $P_2$ . On the basis of the rotational moment law, the relation between the finger pressing (and/or pulling) force and the linear force on the syringe piston is expressed as

$$F_{out} = \frac{2a}{r + 2r \cos \frac{\theta}{2}} F_{in} \quad (2)$$

Equation (2) is plotted as Fig. 5(b), showing that the output/input force ratio is determined by the rotational angle and the ratio between the length and height of the distal phalanx holder.

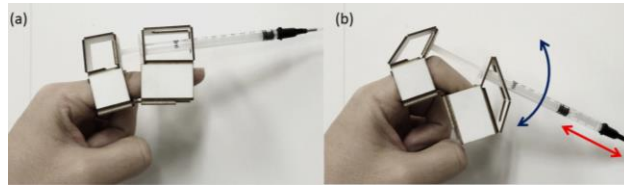


**Fig. 4.** Motion of the index (or middle) finger in the finger exoskeleton. (a) Initial state. (b) Deployed state. The displacement of the syringe is synchronized with the motion of the finger. The blue solid line and the red arrow indicate the rotation of the exoskeleton and the expansion of the syringe, respectively.

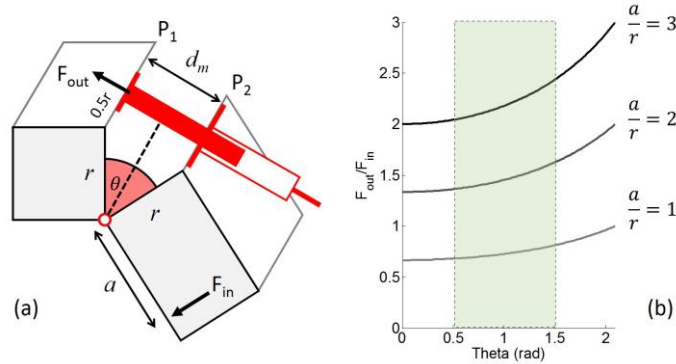


**Fig. 5.** (a) A free-body-diagram of the index finger exoskeleton. The syringe piston is moved by the rotation of the distal phalanx holder. (b) The ratio between the syringe force ( $F_{out}$ ) and the finger force ( $F_{in}$ ) is dependent on the rotational angle ( $\theta$ ) and the ratio between  $a$  and  $r$ , which are the length and the height of the distal phalanx. The green region shows the working range of the finger exoskeleton, between about  $30^\circ$  and  $85^\circ$  degree.

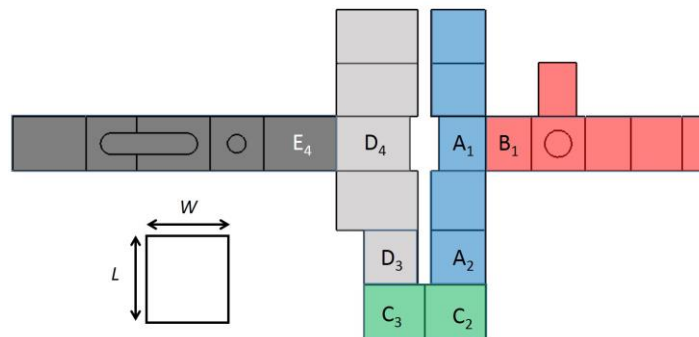


**Fig. 6.** The unfolded crease pattern of the index finger exoskeleton. The red surfaces (B) and the dark-gray surfaces (E) become piston and syringe holders, respectively. The blue-colored surfaces (A) and the light-gray surfaces (D) become phalanx holders. The green surfaces connect two phalanx holders. There are four pairs of connecting surfaces ( $A_1$  and  $B_1$ ,  $A_2$  and  $C_2$ ,  $C_3$  and  $D_3$ , and  $D_4$  and  $E_4$ ).

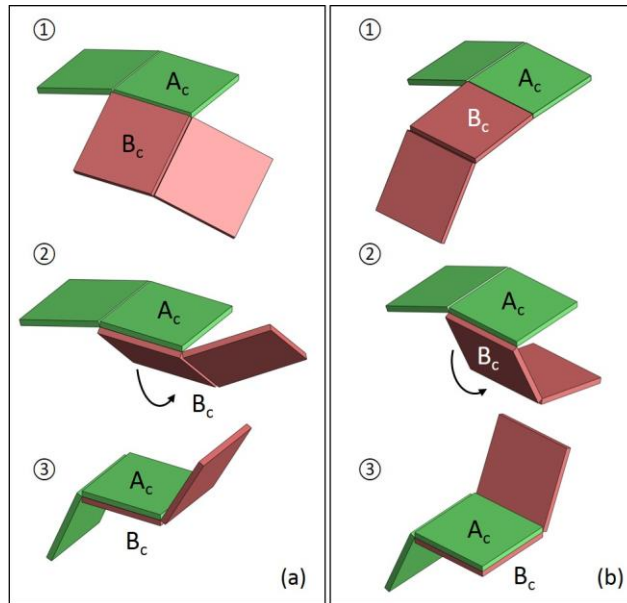


**Fig. 7.** Changing the folding direction of the single-sided foldable structure using the back-to-back folding surfaces ( $A_c$  and  $B_c$ ).

Each exoskeleton component is a folded structure. Figure 6 shows the unfolded crease pattern of the finger exoskeleton consisting of four parts (A, B, C and D). The green surfaces (C) are folded about the center line. The blue surfaces become the rigid rectangular parallelepiped for holding the distal phalanx. The surfaces  $A_2$  and  $C_2$  connecting the parts A and C are folded back-to-back. As a result the surface  $C_2$  is located inside the rigid rectangular parallelepiped. The light-gray surfaces (D) become the rigid rectangular structure for holding the proximal phalanx. The surfaces  $D_3$  and  $C_3$  connecting the parts D and C are folded back-to-back. The surface  $C_3$  is located inside the rigid rectangular parallelepiped. The dark-gray surfaces and the red surfaces become compliant rectangular parallelepipeds, holding the syringe and the piston, respectively. The surfaces  $D_4$ - $E_4$ , and  $A_1$ - $B_1$  are folded back-to-back as the previous connecting surfaces.

The back-to-back folding surfaces play two important roles in the origami structure. First, they change the folding directions of structures, so that complex shape three-dimensional structures are integrated into one and made from one single paper. Figure 7(a)-(b) show simple examples. If the surfaces  $A_c$  and  $B_c$  connecting two parts are folded back-to-back, the folding direction changes after these connecting surfaces. This property was used multiple times when designing the crease pattern of the finger exoskeleton to integrate four rectangular parallelepipeds into one.

Second, it is possible to adjust the rigidity of the 3D structure using the length (and/or width) margin of the connecting surfaces. For example, while the syringe and piston holders are easily slanted by the orientation of the syringe, the phalanx holders are very rigid because the surfaces  $C_2$  and  $C_3$  inside the phalanx holders do not have a length margin for the surrounding structures to move (i.e.,  $L_{C2} = L_{A2}$  and  $L_{C3} = L_{D3}$ ).

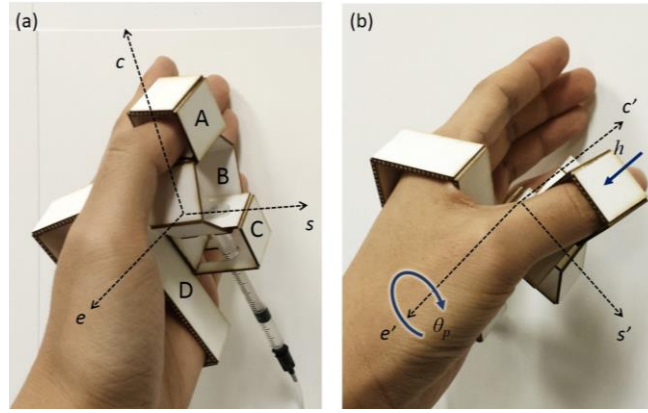


**Fig. 8.** Motion of the thumb in the exoskeleton. (a) Initial state. The dashed lines present the axes ( $c$  and  $e$ ). A: phalanx holder, B: foldable linkages for the syringe's linear motion, C: passive joint, D: palm holder. (b) Compressed state. The right blue arrow indicates the applied force direction (or the moving direction of the piston).  $h$  means the displacement of the piston. The left arrow shows the passive rotation ( $\theta_p$ ) of the connecting joint about the  $e$ -axis.

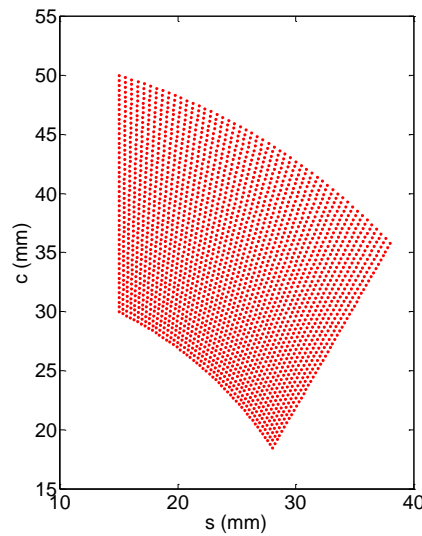


**Fig. 9.** The workspace of the center of the thumb phalanx holder where  $\mathbf{P}_0$  is  $[15 \ 0 \ 30]^T$ , its linear displacement ( $h_a$ ) changes between 0 and 20 mm, and the passive rotational angle ( $\theta_p$ ) changes between  $0^\circ$  and  $30^\circ$ .

### 3.3. Thumb exoskeletons

Thumbs have two short phalanxes of which bending angles are relatively limited. Thus, thumb exoskeletons need a different design from the index finger exoskeleton, considering ergonomics. Figure 8 shows the minimal design for the thumb exoskeleton, which is made of a single paper cardboard. The device holds the operator's palm and distal phalanx using the rigid rectangular structures (D and A), respectively. The syringe piston is pushed (or pulled) in the  $c$ -direction by the thumb holder. The foldable linkages (B) protects this linear motion. The rotational joint (C) connecting the linearly moving parts (A and B) to the palm holder (D) is passively rotated about the  $e$ -axis by the position and orientation the thumb phalanx. This passive joint is

ergonomically important to make operators feel comfortable during operation. Equation (3) shows the matrix form equation to calculate the three-dimensional center of the phalanx holder,  $\mathbf{P}_t = [s_t \ e_t \ c_t]^T$ .

$$\begin{bmatrix} s_t \\ e_t \\ c_t \\ 1 \end{bmatrix} = \begin{bmatrix} \cos \theta_p(t) & 0 & \sin \theta_p(t) & 0 \\ 0 & 1 & 0 & 0 \\ -\sin \theta_p(t) & 0 & \cos \theta_p(t) & 0 \\ 0 & 0 & 0 & 1 \end{bmatrix} \begin{bmatrix} s_0 \\ e_0 \\ c_0 + h_a(t) \\ 1 \end{bmatrix} \quad (3)$$

where  $\theta_p$  is the rotational angle of the passive joint,  $\mathbf{P}_0 = [s_0 \ e_0 \ c_0]^T$  is the initial position of the center of the thumb phalanx holder, and  $h_a$  is the displacement of the syringe piston in the  $c'$ -direction. Fig. 9 shows the two-dimensional workspace of  $\mathbf{P}_t$  considering the design variables of the thumb exoskeleton.

Figure 10 shows the unfolded crease pattern, which consists of four parts including three pairs ( $A_1/B_1$ ,  $B_2/C_2$ , and  $C_3/D_4$ ) of back-to-back folding surfaces. The palm holder has a bi-layer to strengthen the mechanical robustness because it should not be rotated or distorted when the finger pushes (or pulls) the piston. The left foldable line of the surface  $A_1$  is slanted to make the thumb phalanx fit into the holder.

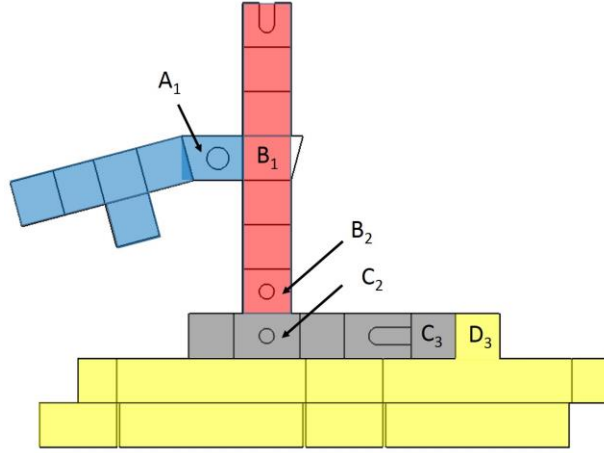


**Fig. 10.** The crease pattern of the thumb exoskeleton. Blue surfaces (A): the phalanx holder. Red surfaces (B): the linear motion linkages. Gray surfaces (C): the passive rotational joint. (D) Yellow surfaces: the palm holder.

### 3.4. Material and manufacturing methods

We used 1.2 mm thickness paper cardboards, which are made of alpha-cellulose pulp from purified wood fiber. The laser-cutting machine engraves or cuts the paper cardboard, following all lines of the designed crease pattern. The laser beam frequency is set low around 280 Hz not to burn the paper. The outer lines are cut through by a high power laser-beam (> 30%). The foldable lines are engraved by a weak laser beam (15-20%). The thickness of the hinge determines its compliance. The stiffness of the flexure hinge is analytically modeled as

$$k_\theta = \frac{Ewt^3}{12l} \quad (4)$$

where  $l$  is the length of the engraved hinge,  $t$  is the thickness,  $w$  is the width into the surface, and  $E$  is the Young's modulus of the paper cardboard (Hoover et al., 2009). This equation presents that the thickness of hinge is the most critical factor to determine its compliance.

Thin flexure hinges have wide bending angles, but their durability is limited because of fatigue failure. Thus, the foldable lines should be engraved by different settings in the laser machine considering their roles in each structures. Figure 11(a)-(c) shows several flexure hinges of different thicknesses. For example, the back-to-back folding surfaces should have very compliant flexure hinges for precise alignment even in a wide bending angle ( $\theta = 180$ ). On the other hand, the slanting rectangular structures (the parts B and E in Fig. 6) and the linear linkages (the part B in Fig. 10) need to have thicker flexure hinges because durability is important and their bending angle is not wide ( $\theta < 90$ ). Thick hinges are destroyed even in a small bending angle because of the material property (Fig. 11(c)).

The reason that single-sided foldable hinges are used in the proposed micromanipulation system is related to the manufacturing process. Technically, it would not be easy to design the crease pattern of 3D origami structures employing only single-sided foldable hinges because the back-to-back folding surfaces should be embedded between patterns. Assuming the use of double-sided foldable hinges, the crease pattern would be easily designed without the integration process. However, both surfaces of paper cardboards have to be engraved (and/or cut) by a laser beam machine, which requires manual intervention between the steps (Yim and Kim et al., 2015). If the paper cardboards are not precisely aligned in the machine, the crease patterns on their both sides have double outlines and foldable lines, and then they are not assembled accurately. This point is particularly disadvantages for manufacturing precision linear motion stages.

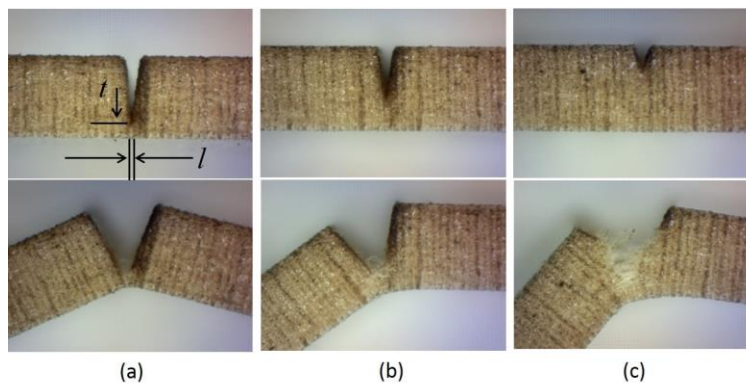


**Fig. 11.** Microscopic images (side view) of the engraved flexure hinges after the laser beam machining (Epilog Zing 30W, US). (a) 100% speed and 20% power:  $t = 1.2$  mm. (b) 100% speed and 15% power: 0.42 mm, and (c) 100% speed and 12% power: 0.85 mm.

## 4. Paper-made slave micromanipulator

### 4.1. Design features

Thick paper cardboards are useful materials for origami-based devices because rigid surfaces are folded accurately about laser-engraved lines, not requiring additional compliant layers for flexure hinges (see Fig. 11). However, their inherent deflection is a major drawback for the material of a precision motion system. We developed two key origami-elements to compensate for this disadvantage.

The first element is *Sarrus* linkage mechanism (Fig. 12(a)). Three pairs of foldable surfaces allow the precise linear motion of the surface S, preventing its rotation or translation in other directions. Its translational stiffness in the  $x$ - and the  $z$ -direction are, respectively, expressed as

$$k_x = \frac{Et w_R^3}{3l^3} \quad (5)$$

$$k_z = \frac{2E t h_R^3}{3l^3} \quad (6)$$

where  $w_R$  and  $h_R$  are the width and the height of the surface R. Geometrically, the ratios  $w_R l^{-1}$  and  $h_R l^{-1}$  are very high, and the translational stiffness,  $k_x$  and  $k_z$ , are proportional to the third order of them.

The second key element is the bilayer cantilever with the folded side surface (Fig. 12(b)). The lower layer (F) removes the residual stress of the upper layer (E) first. Straightness propagate along the folded line between the side surface (G) and the upper surface. The bending stiffness of this structure about the  $x$ -axis is expressed as the equation (7). The first term and the second term indicate the effect of the bilayer cantilever and the folded side surface, respectively.

$$R_x = \frac{8E w_E \delta^3}{12s} + \frac{E \delta w_G^3}{12s} \cong \frac{E \delta w_G^3}{12s} \quad (7)$$

The stiffness of this origami-element is about 315 times bigger than that of the single layer cantilever where  $w_e$  is 20mm,  $\delta$  is 1.2 mm,  $s$  is 65 mm, and  $w_g$  is 20mm.

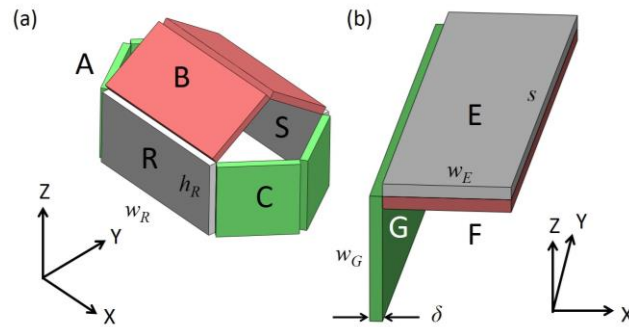


**Fig. 12.** Critical elements of the linear motion stages. (a) *Sarrus* linkage mechanism. The surface S moves linearly from the reference surface, R, under the guidance of three pairs of foldable surfaces A, B, and C. (b) The bilayer cantilever, E and F, with the folded side surface, G, improves the straightness of the cantilever.

The micromanipulator consists of four linear motion stages (Fig. 13). The  $x$ -,  $y$ - and  $g$ -motion stages are integrated together ( $g$  means grippers). The  $z$ -motion stage is separated from the other motion stages, and has a cantilever, the arena of micro objects. All motion stages are above the flat metallic surface with a low friction force. This single-storey micromanipulator minimizes the deflection of the motion stages due to their weights. Figure 14 describes the connection of the motion stages using a simplified schematic diagram. The active  $x$ -stage and the passive  $x$ -stage are fixed on the metallic plate by small magnets. The passive  $x$ -stage ( $X_p$ ) at the opposite side does not have a syringe, and only assists the linear motion of the active  $x$ -stage ( $X_a$ ) not to be bent. The two  $x$ -stages move the attached wide flat plate in the  $x$ -direction where the  $y$ -motion stage (Y) is fixed at one edge of the plate. The  $y$ -motion stage moves the attached  $g$ -motion stage (G) in the  $y$ -direction. As a result, the gripper stage slides on the plate in the  $x$ - and  $y$ -directions by  $X_a$ ,  $X_p$  and Y. The  $g$ -motion stage (G) provides one degree-of-freedom to one gripper on the cantilever

(the other gripper on the other cantilever is stationary). The  $z$ -motion stage has three pairs of linkages folding in three directions in equilibrium, which minimizes the deflection of the top surface. Micro objects are located on the long bilayer cantilever connected the top surface of the  $z$ -motion stage.

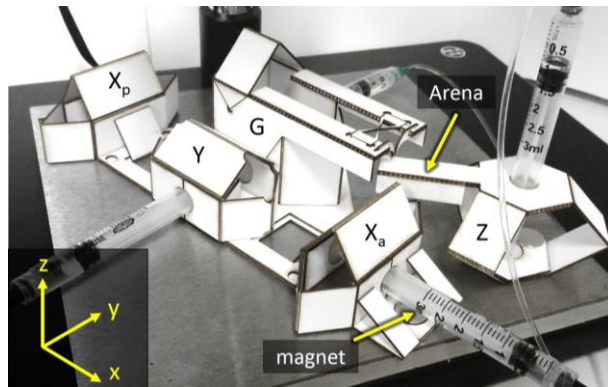


**Fig. 13.** A photograph of the origami-based paper-made micromanipulator (four degree-of-freedom) on the flat metallic plate.  $X_p$  and  $X_a$ ,  $Y$ ,  $Z$  and  $G$  are the  $x$ -,  $y$ -,  $z$ - and  $g$ -motion stages, respectively. The coordinate is presented on the lower-left corner.

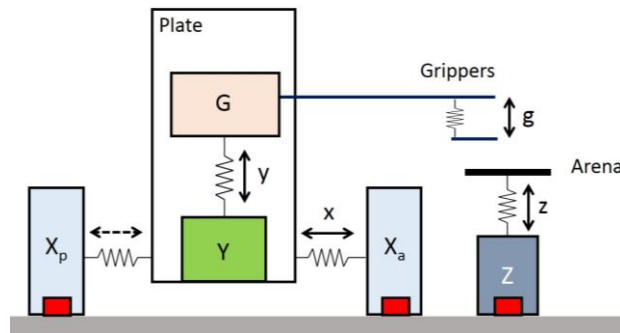


**Fig. 14.** A connection diagram of the motion stages.  $X_a$  and  $X_p$  are fixed on the surface by the magnets (red). The manipulator tip is movable in the  $x$ -, and  $y$ -directions, and  $G$  provides one more degree of freedom for the grippers' motion.

Figure 15(a)-(d) show the unfolded crease pattern of the motion stages. The  $x$ -stage has one pair of back-to-back folding surfaces to change the folding direction. All stages employ *Sarrus* linkage mechanism. The  $y$ -,  $z$ -, and  $g$ -stages have the orthogonal bi-layer structure. The cantilever of the  $z$ -stage becomes the arena for micro objects to be manipulated. Grippers are fixed in the slots in the  $g$ -stage cantilever.

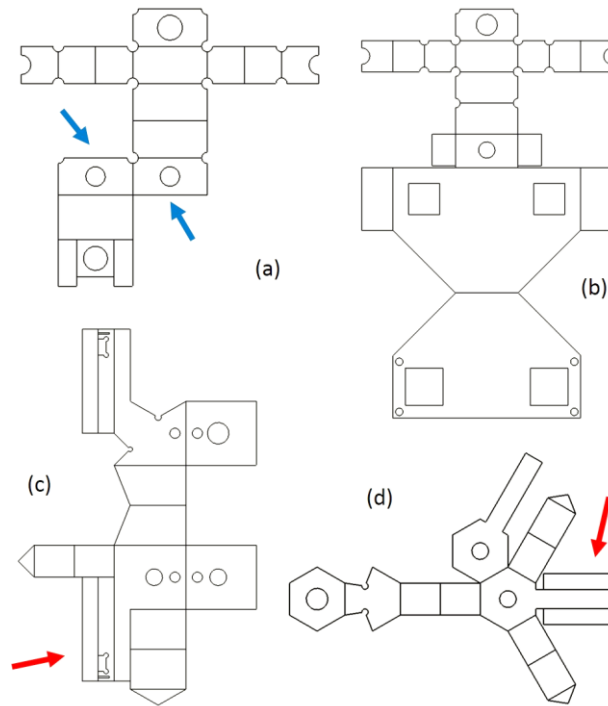


**Fig. 15.** The crease pattern of the motion stages. (a) The active  $x$ -motion stage. The blue arrows indicate the back-to-back folding surfaces. (b) The  $y$ -motion stage. (c) The  $g$ -motion stage. (d) The  $z$ -motion stage. The red arrows present the bilayer cantilever with an orthogonally folded side surface. All figures are not drawn to scale.

## 4.2. Grippers

Grippers are critical in performing advanced micromanipulation tasks such as pick-and-place and 3D micro-assembly. In accordance with the design paradigm of printable programmable robots, we developed two kinds of paper-made grippers, which are mass-producible with laser cutting machines, replaceable, customizable, and fixed with the  $g$ -motion stage without adhesives.

*i) Laser-machined 2D grippers:* vertical grippers are orthogonally fixed to the cantilever using small slits (see A in Fig. 16). They are arc-shaped, so that their sharp tips do not touch other micro objects on the arena during manipulation. The horizontal grippers have a trapezoidal shape, and their inner-surface is cut to secure the sight of the microscope (see B in Fig. 16). Both vertical and horizontal grippers are manufactured by using a laser cutting machine.  $200\ \mu\text{m}$  is the minimum width of the grippers to maintain their mechanical strength for gripping micro objects. Using our current fabrication method and equipment (Epilog Zing laser series 30W), it is difficult to make grippers thinner than this dimension because the burning effect of the laser beam ruins the designed geometry.

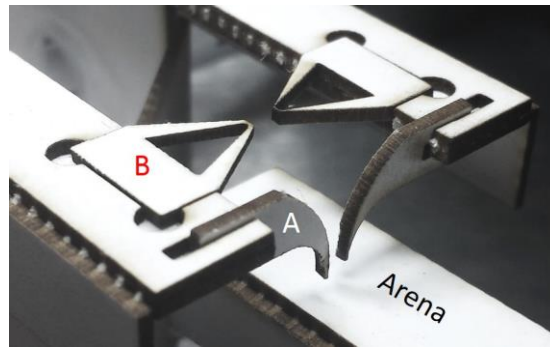


**Fig. 16.** Laser-machined 2D grippers fixed on the bilayer cantilever of the  $g$ -motion stage. A: hook-shaped vertical grippers. B: Trapezoidal-shaped horizontal grippers. The long bilayer cantilever of the  $z$ -motion stage becomes the arena for micro objects to be manipulated.

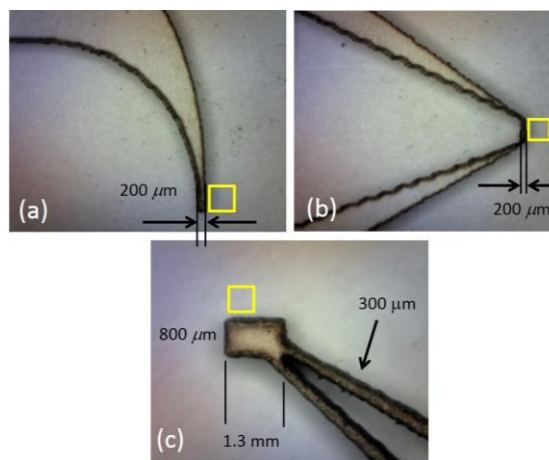


**Fig. 17.** Microscopic images of the laser-machined grippers. (a) Hook-shaped gripper (side-view) (b) Trapezoidal horizontal gripper (top-view). (c) Chopstick-shaped horizontal gripper (top-view). The yellow boxes show the position of  $500 \mu\text{m}$ -sized micro objects.

ii) *Origami-based compliant 3D grippers*: origami engineering allows fabrication of compliant 3D grippers, which have two benefits than the 2D grippers. First, the shape of their tips is customizable according to the shape of the object to be manipulated. Second, the stress on the manipulated objects is minimized because thin film-made grippers are slightly deformed by the interaction with objects. These features are useful to grip fragile or biological materials. Figure 18 and 19 depict origami-inspired compliant 3D grippers and the crease pattern, respectively. The geometry is designed such that the tip angle of the gripper can be instantly varied with a minimal modification in the design, i.e.,  $\alpha$ , whereas keeping two  $\beta$  the same angle ensures that the surface can be folded full-flat thus the mechanical latches function to solidify the structure, permitting minimum deformation when grabbing an object. On the other hand, by releasing the latches, the grippers gain certain compliance for soft handling of an object. An observing window was added to visually capture awaiting micro objects under the cantilever to be assembled. The employed manufacturing process is the same as in Section 3.4., with a weaker set of laser power (5%). The assembly was made by manually folding along the creases without any usage of tools or adhesives. Except a latching process which requires deformation of a sheet material, the assembly process can also be performed by self-folding technique (Miyashita et al., 2014; Tolley et al., 2014).

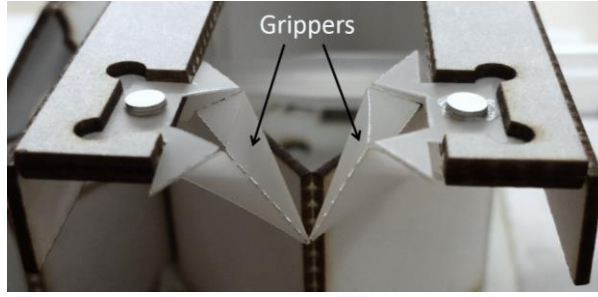


**Fig. 18.** Origami-inspired thin grippers fixed to the cantilever of the gripper stage.

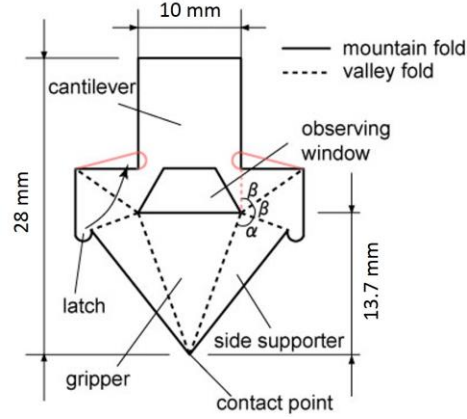


**Fig. 19.** The unfolded crease pattern of the origami-inspired grippers. The design variables:  $\alpha = 90^\circ$  and  $\beta = 85^\circ$ .

### 4.3. Hydraulic motion reduction

Each motion stage of the micromanipulator is moved by the hydraulic motion reduction mechanism using two syringes of different diameters. Compression and expansion of the master syringe in the finger exoskeleton enables expansion and compression of the slave syringe in the manipulator, respectively. Assuming that water is incompressible and not vaporized inside the syringe, the displacements of the pistons in two syringes are inversely proportional to their cross-sectional area ratio. Equations (8) and (9) show linear displacements of the motion stages as a function of the corresponding finger motion, respectively.

$$\Delta d_s = 2r\alpha \left( \sin \frac{\theta_{m,t}}{2} - \sin \frac{\theta_{m,0}}{2} \right) \quad (x, y, \text{ and } g - \text{stages}) \quad (8)$$

$$\Delta d_s = \alpha \Delta d_{m,thumb} \quad (z - \text{stage}) \quad (9)$$

where  $\alpha$  is the cross-sectional area ratio between the master syringe cylinder and the slave syringe cylinder. Table 2 shows the look-up-table about the motion of each finger and the moving direction of the corresponding motion stage.

**Table 2.** Look-up-table about the moving direction of the manipulator tip by the finger motion.

	<i>Bending motion</i>	<i>Straightening motion</i>
Left index	-Y	+Y
Left middle	+X	-X
Left thumb	-Z	+Z
Right index	gripping	releasing

The employed hydraulic motion reduction system has a single-acting-unit, without a compressible spring preloading the piston in the opposite direction. We experimentally evaluated whether this motion reduction system is repeatable and consistent. We attached different weights (50g, 100g and 200g) to the piston bottom to cause an external load, continuously repeated full expansion ( $\theta_m = 100^\circ$ ) and full compression ( $\theta_m = 20^\circ$ ) of the index finger exoskeleton twenty times in each condition, and measured the position of the piston in the slave syringe. Table 3 shows the average and standard deviation of the gradients between two points, presenting that the motion reduction ratio is consistent even when the external load is applied to the system.

**Table 3.** Hydraulic motion reduction between the index finger exoskeleton and the motion stage.

$F_{load}$ (mN)	$(d_{s,max} - d_{s,min})(\theta_{m,max} - \theta_{m,min})^{-1}$ [mm/degree]
-490	- 0.075 $\pm$ 0.0029
-980	- 0.078 $\pm$ 0.0022
-1960	- 0.078 $\pm$ 0.0045

The hydraulic motion reduction mechanism allows force transmission between the operator and the manipulated object. Note that this is applicable only when compressing the master syringe. Equation (10) shows the relation of forces produced in two syringes when compressing the master syringe.

$$F_{master} = D + V + \alpha(S + F_{slave}) \quad (10)$$

where  $F_{master}$  is the applied force to the piston in the master syringe,  $D$  is the frictional force between the master syringe and the piston,  $V$  is the viscous friction between the flowing water and the internal surfaces of syringes and a tube,  $S$  is the frictional force between the slave syringe and the piston, and  $F_{slave}$  is the output force of the piston at the slave syringe. This equation presents that  $F_{slave}$  is proportional to  $F_{master}$ , and the ratio is constant.

We investigated the force transmission between the master and slave syringes in experiments. They are fixed in the air by holders, and load cells are attached to pistons respectively (Fig. 20(a)). A compliant object was placed between the slave syringe piston and the bottom surface. We pressed the master syringe piston, and measured the forces ( $F_{master}$  and  $F_{slave}$ ) using the load cells. The experiments were repeated after changing the compliant object to a rigid one. The experimental results show two analysis (Fig. 20(b)). First, the interaction force between the slave syringe piston and the object is linearly proportional to the applied force to the master syringe piston. The gradient of the plot is about 3.72, and consistent regardless of the compliance of the object below the slave syringe piston. The cross-sectional area ratio of the two syringes is 1:4.2. Considering the measurement noise and the error due to the inflation of the tube, the experimental results are consistent with the theory. Second, the total frictional force in the hydraulic system is around 1 N. If the applied force becomes higher than 1N (see the dashed-line

box in Fig. 20(b)), the piston slightly starts to move because of the inflation of the water-filled tube or the deformation of the object. The linear relation between  $F_{\text{slave}}$  and  $F_{\text{master}}$  is valid only when the applied force is stronger than this inherent load.

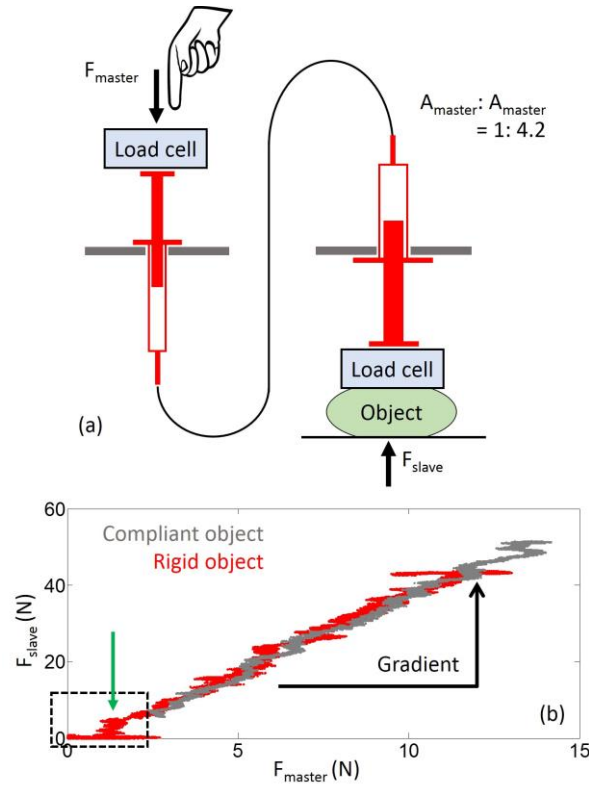


**Fig. 20.** Force transmission experiments. (a) A schematic figure of the experimental setup for measuring the interaction forces. The cross-sectional area ratio of the two syringes is 1:4.2. (b) The interaction force ( $F_{\text{slave}}$ ) between the slave syringe piston and the object is proportional to the applied force ( $F_{\text{master}}$ ) to the master syringe piston regardless of the compliance of the objects. The green arrow indicates the sum of the frictional forces modeled in the equation 10.

## 5. Experiments

This section describes experimental results for micromanipulation with our system. All demonstrations are included in the supplementary multimedia file. The operator was trained for two hours to become familiar with the mobility and the moving direction of the manipulator in the displayed video images. As the operator's skill and experience improved, finally, the success/failure ratio became higher than 80%.

*i) Motion precision:* first, we evaluated the straightness of each motion stage and  $xy$  orthogonality (Fig. 21). We placed a small ink-jet printed circle (diameter: 1.2 mm) on the cantilever of the  $g$ -motion stage, and manipulated it using the finger exoskeletons. Figure 21(a)-(c) show the centroid of the circle while the manipulator is moved in the  $z$ -,  $x$ - and  $y$ -directions, respectively. We defined that the straightness is the maximum gap distance between two lines moving back and forth divided by the one-way length during the linear round trip. The angle between two lines moving in the  $x$ - and  $y$ -directions presents the orthogonality (Fig. 21(d)). The experiments were repeated three times in each case, and the results are summarized in Table 4. The straightness and the  $xy$  orthogonality of the linear motion stages are also affected by the precision in assembly and alignment of parts. Technically,

however, 0.25 – 0.96% straightness and the orthogonality error below 0.5° are achievable only when i) the deflections of paper cardboards are compensated by using the presented origami elements, and ii) the origami-based linkages mechanisms guide the linear motion of the stages precisely.

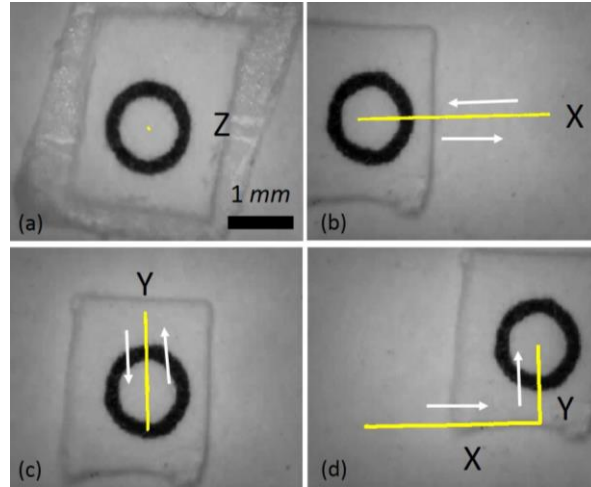


**Fig. 21.** Straightness of the motions and the XY-orthogonality. The yellow lines present the tracked positions of the circle centers, which are detected by using image processing techniques. (a) The z-axis motion. This shows extremely small displacement of the circle center as a dot. (b) The x-axis motion (c) The y-axis motion (d) xy orthogonality. In all figures, the white arrows indicate the moving direction of the circle centers.

**Table 4.** The motion precision of each stage

<i>Straightness of the motion stages</i>		<i>XY orthogonality</i>
X	$0.0030 \pm 0.0004$	$89.5 \pm 0.96$ [deg]
Y	$0.0025 \pm 0.0012$	
Z	$0.0096 \pm 0.0004$	

ii) *2D trajectory following*: we set three letters, MIT, on the arena, and controlled the micromanipulator tip to follow the letters (width: 400 μm). Figure 22 shows the trace of the manipulator tip (width: 400 μm) on the reference trajectory. Following the horizontal and vertical lines is very stable. Moving in the diagonal direction is difficult because the x-axis motion and the y-axis motion should be combined.

iii) *Pick-and-place and 3D micro-assembly*: assembling micro objects in 3-D is an advanced task. We prepared two kinds of cubic micro objects, 1 mm-sized ones and 500 μm-sized ones (Leong et al., 2007; Pandey et al., 2013), and manipulated bigger ones with the early version of the origami-based micromanipulation system (Yim et al., 2015). Multiple micro objects are randomly distributed at the beginning, organized to one-by-four formation, two-by-two formation and finally four-by-one formation.

iv) *Micro separation and 3D micro-assembly*: manipulating some of multiple micro objects without touching the rest ones is a higher level demonstration because the untouchable objects become obstacles limiting the path of the grippers. The vertical grippers in Fig. 16 are useful in this manipulation task because their small tips do not conflict other micro objects on the arena. We set multiple micro objects in a small space (Fig. 24(a)). Assuming that the object A should not be touched during

manipulation, we picked up B between A and C (Fig. 24(b)), and placed it on A (Fig. 24(c)). Next, the object C is pushed to the safe area by the tip (Fig. 24(d)). The stacked micro objects are hidden by the gripper, but not touched. In the safe area, we picked up C (Fig. 24(f)), and place it on B again (Fig. 24(g-h)).

v) *Origami-based compliant 3D grippers*: unlike the laser-machined 2D grippers, the 3D origami grippers are very compliant because they are made of a thin film ( $100\ \mu\text{m}$ ). They are passively deformed by the interaction with micro-object, so that they are more appropriate for manipulating fragile or biological materials. In the experiments, the sharp tips go into the hollow surface of the object. Technically, they are disadvantages when gripping a geometrically flat micro-object. However, the shape of the tips could be adjusted according to the shape of the objects.

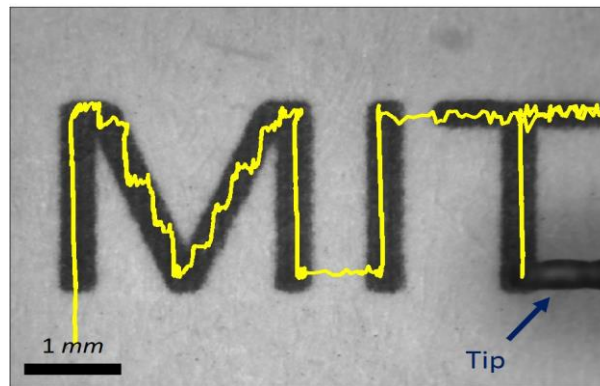


**Fig. 22.** 2D trajectory following experiments. Three letters, MIT, are the reference. The yellow line indicates the tracked position of the manipulator tip.

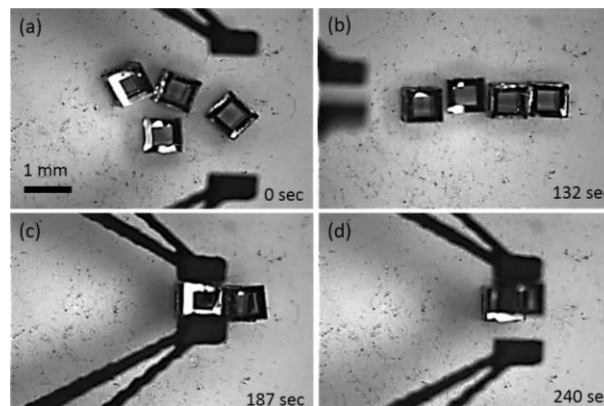


**Fig. 23.** Pick-and-place and 3D assembly of multiple micro objects. (a) Micro objects are randomly distributed at the beginning, (b) organized to one-by-four formation, (c) two-by-two formation, and (d) finally four-by-one formation. The time lapse are shown in the lower-right corners.

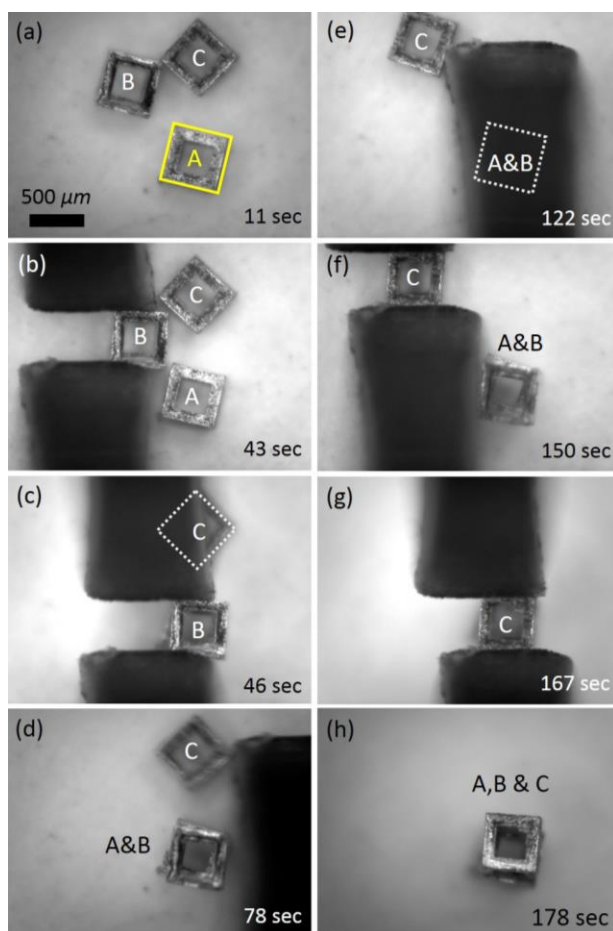


**Fig. 24.** Delicate separation and 3D assembly of multiple micro objects ( $500\ \mu\text{m}$ ) using the vertical grippers. The time lapse are shown in the lower-right corner. (a) Three micro objects are in the small space. The object A in the yellow box should not be touched during manipulation. (b) Picking-up B between A and C. (c) Placing B on A. (d-e) Pushing C to a safe area with the tip. (f) Picking up C. (g-h) Placing C on A and B.

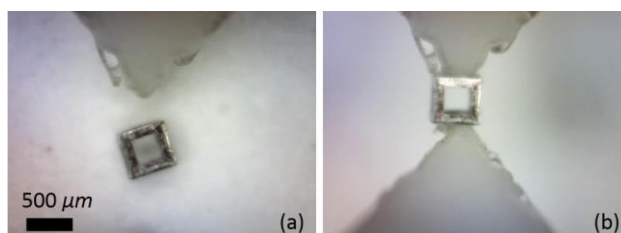


**Fig. 25.** Picking up a  $500\ \mu\text{m}$ -size object with the compliant 3D grippers.

## 6. Discussion

This research contributes a rapid design and fabrication method for a low-cost high-performance micromanipulation system employing three-dimensional origami technologies. We envision users downloading appropriate cut-and-crease patterns from on-line stores, and rapidly prototyping a customized system using inexpensive off-the-shelf materials and a laser cutting machine. The design is customizable to adjust the manipulation resolution (e.g., a few millimeters to tens of micrometer). Users can

achieve different parameters for their specific applications by changing the combination of the syringes. The time required to build the entire micromanipulation system is less than one hour.

The developed micromanipulation system shows a range of different high level micromanipulation abilities in experiments. In the current version, however, operators cannot feel the hydraulic feedback force during the gripping motion yet because of two reasons. First, the force transformation ratio is 0.27, so that operators can feel only a small part of the feedback force. Second, the interaction force is lost by the deformation of the long cantilever of the gripper stage. A new design of the micromanipulation system with hydraulic haptic feedback is the topic of the future research.

In this paper, we used a commercial microscope to view micro objects and their manipulation. In accordance with the printable programmable robot paradigm, this system would be replaceable with a mobile smartphone with an attachable microscope lens. Commercial micro scope lens for smart phones cost only 10 – 20 US dollars. Also, it is possible to manufacture the lens using a drop of glue (or a transparent polymer) as studied in (Cybulski et al., 2014). The total cost of the current system excluding the microscope is less than five US dollars for the current design, using current prices (Table 5).

**Table 5.** The bill-of-material of the origami-based paper-made micromanipulation system

<i>Material</i>	<i>unit price × number</i>
Paper cardboard (L 500 mm × H 800 mm size)	\$2.3 × 1
Syringes	\$0.07 × 8
Magnet (D 12.3 mm × T 1.6 mm)	\$0.81 × 2
Total: \$4.48	

## 7. Conclusion

This paper presents the first low-cost (i.e., bill-of-materials smaller than five US dollars), high performance (i.e., capable of doing pick-and-place, 3D micro assembly, and micro objects separation), precision (i.e., 0.25 – 0.96% straightness and  $89.5 \pm 0.96^\circ$   $xy$  orthogonality) origami-inspired tele-micromanipulation system. We described the critical origami structures, the crease pattern design process, and the planar manufacturing methods for creating the system. Finally, we evaluated the functionalities of the developed system in experiments. The current system is the result of multiple design modification achieving a range of high level micromanipulation tasks. However, operators can improve (or modify) the proposed design further according to their specific applications in addition to the useful origami structures that we proposed in this paper. The working ranges and resolution are also customizable by changing the combination of syringes in the presented hydraulic motion reduction system.

## Acknowledgement

The authors would like to thank David H. Gracias and Shivendra Pandey for providing micro objects required for experimental demonstrations.

## Funding

This work was supported by the National Science Foundation, grant numbers 1240383 and 1138967

## References

- An B, Miyashita S, Tolley MT et al. (2014) An end-to-end approach to making self-folded 3D surface shapes by uniform heating. In: *Proc. of the 2014 IEEE International Conference on Robotics and Automation (ICRA)*, pp.1466-1473.
- Bhattacharyya B, Doloi B, and Sridhar PS (2001) Electrochemical micro-machining: new possibilities for micro-manufacturing. *Journal of materials processing Technology* 113(1): 301-305.
- Boeckx W (1976) Clinical micro-surgery. Micro-surgery. Experimental techniques in the rat and clinical applications. *European Press*, Ghent, Belgium, 192-194.
- Caron AW, Massie B, and Mosser DD (2000) Use of a micromanipulator for high-efficiency cloning of cells co-expressing fluorescent proteins. *Methods in cell science* 22(2): 137-145.
- Causa F, Netti PA, and Ambrosio L (2007) A multi-functional scaffold for tissue regeneration: the need to engineer a tissue analogue. *Biomaterials* 28(34): 5093-5099.
- Cybulski JS, Clements J, and Prakash M (2014) Foldscope: origami-based paper microscope. *PLoS ONE* 9(6), e98781.
- Felton S, Tolley MT, Demaine E et al. (2014) A method for building self-folding machines. *Science* 345(6197): 644–646.
- Felton SM, Tolley MT, Onal CD et al. (2013) Robot self-assembly by folding: A printed inchworm robot. In: *Proc. of IEEE International Conference on Robotics and Automation (ICRA)*, pp.277-282.
- Gauthier M and Piat E (2006) Control of a particular micro-macro positioning system applied to cell micromanipulation. *IEEE Transactions on Automation Science and Engineering* 3(3): 264-271.
- Hale LC (1999) Principles and techniques for designing precision machines. Ph.D. dissertation, Massachusetts Institute of Technology.
- Hawkes E, An B, Benbernou NM et al. (2010) Programmable matter by folding. *Proceedings of the National Academy of Sciences* 107(28):12441-12445.
- Hoover AM, and Fearing RS (2009) Analysis of off-axis performance of compliant mechanisms with applications to mobile millirobot design. In: *Proc. of IEEE/RSJ International Conference on Intelligent Robots and Systems (IROS)*, pp.2770-2776.
- Inoue K, Arai T, Tanikawa T et al. (2005) Dexterous micromanipulation supporting cell and tissue engineering. In: *Proc. of IEEE International Symposium on Micro-NanoMechatronics and Human Science*, pp.197-202.
- Kawase Y, Iwata T, Watanabe M et al. (2001) Application of the piezo-micromanipulator for injection of embryonic stem cells into mouse blastocysts. *Journal of the American Association for Laboratory Animal Science* 40(2): 31-34.
- Leong TG, Lester PA, Koh TL et al. (2007) Surface tension-driven self-folding polyhedral. *Langmuir* 23(17): 8747–8751.
- Mehta A, Bezzo N, An B, et al. (2014) A design environment for the rapid specification and fabrication of printable robots. In: *Proc. 14th International Symposium on Experimental Robotics (ISER)*.
- Mehta AM, Rus D, K. Mohta et al. (2013) A scripted printable quad-rotor: rapid design and fabrication of a folded MAV. In: *Proc. of the 16th International Symposium of Robotics Research (ISRR)*.
- Miyashita S, Meeker L, Tolley MT et al. (2014) Self-folding miniature elastic electric device. *Smart Materials and Structures* 23(9).
- Onal C, Wood RJ, and Rus D (2011) Towards printable robotics: origami-inspired planar fabrication of three-dimensional mechanisms. In: *Proc. of IEEE International Conference on Robotics and Automation (ICRA)*, pp.4608-4613.
- Pandey S, Gultepe E, and Gracias DH (2013) Origami inspired self-assembly of patterned and reconfigurable particles. *Journal of Visualized Experiments* (72).
- Popa DO, and Stephanou HE (2004) Micro and mesoscale robotic assembly. *Journal of manufacturing processes* 6(1): 52-71.

- Rebec GV, Langley PE, Pierce RC et al. (1993) A simple micromanipulator for multiple uses in freely moving rats: electrophysiology, voltammetry, and simultaneous intracerebral infusions. *Journal of neuroscience methods* 47(1): 53-59.
- Shimada E, Thompson JA, Yan J et al. (2000) Prototyping millirobots using dextrous microassembly and folding. In: *Proc. of ASME IMECE/DSCD*.
- Soltero DE, Julian BJ, Onal CD et al. (2013) A lightweight modular 12-dof print-and-fold hexapod. In: *Proc. of IEEE/RSJ International Conference on Intelligent Robots and Systems (IROS)*, pp.1465-1471.
- Tabarés JC, MacLachlan RA, Etensohn, CA et al. (2010) Cell micromanipulation with an active handheld micromanipulator. In: *Proc. of the Annual International Conference of the IEEE on Engineering in Medicine and Biology Society (EMBC)*, pp. 4363-4366.
- Tan KK, and Ng SC (2001) Computer controlled piezo micromanipulation system for biomedical applications. *Engineering Science & Education Journal* 10(6): 249-256.
- Thompson JA, and Fearing RS (2001) Automating microassembly with ortho-tweezers and force sensing. In: *Proc. of IEEE/RSJ International Conference on Intelligent Robots and Systems (IROS)*, pp. 1327-1334.
- Tolley MT, Felton SM, Miyashita S et al. (2014) Self-folding Origami: shape memory composites activated by uniform heating. *Smart Materials and Structures* 23(9), 094006.
- Van Steirteghem A (1994) IVF and micromanipulation techniques for male-factor infertility. *Current Opinion in Obstetrics and Gynecology* 6(2):173-177.
- Yaşargil M (2006) *Microsurgery: applied to neurosurgery*. Thieme.
- Yim S and Kim S (2015) Printable, foldable and wearable tele-micromanipulation device for micro-robotic application, In: *Proc. of IEEE International Conference on Robotics and Automation*, to appear.